Robotica (2016) volume 34, pp. 226–242. © Cambridge University Press 2014
doi:10.1017/S0263574714001283

Kinematics and cooperative control of a robotic spinal surgery system

Haiyang Jin†, Ying Hu§¶, Wei Tian‡*, Peng Zhang§¶, Zhangjun Song§¶, Jianwei Zhang‖ and Bing Li†*

†*Shenzhen Graduate School, Harbin Institute of Technology, Shenzhen, China*
§*Guangdong Provincial Key Laboratory of Robotics and Intelligent System, Shenzhen Institute of Advanced Technology, Chinese Academy of sciences, Shenzhen, China*
¶*The Chinese University of Hong Kong, Hong Kong, China*
‡*Department of Spine Surgery, Beijing Jishuitan Hospital, Tsinghua University, Beijing, China*
‖ *Department of Informatics, University of Hamburg, Hamburg, Germany*

(Accepted April 24, 2014. First published online: June 18, 2014)

SUMMARY
Spinal surgery is considered a high-risk surgery. To improve the accuracy, stability, and safety of such operations, we report the development of a novel six-degrees-of-freedom Robotic Spinal Surgical System that can assist surgeons in performing transpedicular surgery, one of the most common spinal surgeries. After optimization performed using Response Surface Methodology, the largest available workspace of the robot is determined and is found to easily cover the entire operation area. Cooperative control and navigation-based active control are implemented for different processes of the operation. We propose a hybrid control approach based on the speed and torque interface at the joint level. In this mode, the robot is compliant in Cartesian space, benefitting both the accuracy and efficiency of the operation. A comprehensive assessment index, combining the subjective and objective criteria in terms of positioning and operation efficiency, is proposed to compare the performance of cooperative control in speed mode, torque mode, and hybrid control mode. Active fine adjustment experiments are carried out to verify the positioning accuracy, and the results are found to satisfy the requirements of operation. As an application example, a pedicle screw insertion experiment is performed on a pig vertebral bone, demonstrating the effectiveness of our system.

KEYWORDS: Robotic spinal surgical system; Spinal surgery; Kinematics; Workspace analysis; Cooperative control; Comprehensive assessment index.

1. Introduction

Robot-assisted orthopedic surgery has received much attention in recent years due to its many advantages, such as high precision, high stability, micro-invasion, rapid recovery and effective reduction of surgeons' work. Combined with image-based intraoperative navigation, surgical robots can assist surgeons in performing various types of surgery, including maxillofacial, dental, joint replacement, spinal surgeries, etc. Of all orthopedic surgeries, spinal surgery is considered one of the highest risk ones due to the many important organs, vessels, and nerves surrounding the human vertebrae in the narrow operation space. If these surrounding tissues are damaged during the operation, irreparable harm to the patient may occur. One of the most common spinal surgeries is transpedicular fixation, which is used to add extra support and enhance the stability of the spine. In this operation, bone screws are implanted into the vertebrae and two rods are fixed on these screws to secure the spine. The screw path begins at the vertebral lamina, passing into the vertebral body through a narrow pedicle. The width of the pedicle is usually 7.8–13.4 mm for lumbar vertebrae, and only 6–8.8 mm for cervical vertebrae. The structure of the vertebrae is shown in Fig. 1.[1,2] To insert a Φ4 mm screw into

* Corresponding author. E-mail: tianweia@vip.163.com, libing.sgs@hit.edu.cn

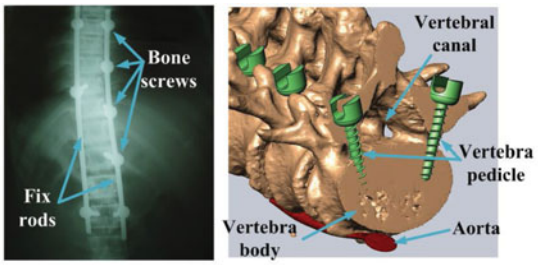

a) Scheme of the operation b) Structure of the vertebrae

Fig. 1. Diagram of screw paths on the vertebrae.

a lumbar vertebra or a Φ3 mm screw into a thoracic vertebra, the screw path error should be less than 1.5 mm, as greater deviation could injure important nerves and blood vessels. In some cases more than 20 screws need to be inserted. During lengthy operations, a surgeon's increased hand tremor and tiredness increase the risk of injury. To reduce these surgical risks, a Robotic Spinal Surgery System (RSSS) capable of safe, stable, controlled movement is desirable.

The RSSSs developed in recent years can be classified into two basic configurations: parallel and series. The SpineAssist parallel robot (Mazor Robotics, Israel) is the only robot in the market with FDA and CE certification.[3,4] The system contains a Stewart-platform parallel manipulator with six degrees of freedom (6 DoFs), a guide rod fixed on the moving platform, a bracket system and planning software. Intraoperatively, the parallel robot is mounted on the patient's spine, automatically adjusting its posture based on the preoperative planning information and placing the guide rod along the planned screw path. The surgeon can manually perform the drilling process expediently through the guide rod[5,6] with the assistance of the robotic system. Another 6-DoF Stewart-platform parallel robotic system, developed by Sun *et al.* (Harbin Institute of Technology, China) is used in cervical disc replacement surgery.[7] A milling tool, fixed to the moving platform, mills through the cervical vertebrae. A similar configuration is used in the URS Evolution 1 surgical robot (Fraunhofer Institute, Germany).[8] The manipulator in this system is made of a universal Stewart-platform parallel robot with an automatic bone drill. An alternative to the Stewart-platform parallel robot is the Neuroglide (École Polytechnique Fédérale de Lausanne, Switzerland), a 4-DoF passive parallel robot used for cervical spine surgery.[9] In this system, two moving arms are connected by a guide rod, constituting a parallel kinematic chain. A robot's DoFs are along the y and z axes and around angles α and β. Using the parallel configuration these robots are relatively small and light, but they are limited to smaller workspaces and can only operate on one area of vertebrae once mounted.

Most robotic systems used in spinal surgery use a serial rather than parallel configuration. An early example of this kind of robot is the pedicle screw placement system developed by Santos-Munné *et al.* (Northwestern University, USA),[10] which uses the PUMA 560 6-DoF industrial robot to perform the positioning and drilling process. The Wallace-Kettering Neuroscience Institute has a similar system based on a Motoman industrial robot.[11] Melo *et al.* (University of Navarra, Spain) use a PA-10 industrial robotic arm as the manipulator in their system.[12] Because these robots were not initially designed for medical applications, they are too big and heavy for use in the operating room. Two types of lightweight robotic arms, named VectorBot, have therefore been developed for pedicle replacement (German Aerospace Center).[13,14] One is based on the universal 7-DoF LWR-II, and the other is the 7-DoF KineMedic, which weighs less than 10 kg. The joints of these lightweight and industrial robots are rotational, so they have a larger workspace and improved dexterity. However, gravity compensation is not considered in their configuration design. If the robot's joints are accidentally over-sped, the robotic arm may drop down and harm the patient's body.

Considering these issues, some researchers have tried to design a more appropriate configuration to guarantee safety during operations. Some Cartesian coordinate robots have been proposed, in which only one joint moves in the vertical direction, thus reducing the possibility of injury. Examples include the 5-DoF Robot-Assisted System for minimally invasive spinal surgery (Nankai University, China),[15] the 5-DoF SPINEBOT-I system (Hanyang University, Korea),[16,17] and the 5-DoF CoRASS (Pohang University of Science and Technology—POSTECH, Korea).[18,19] However, the linear rails or brackets of these robots take up a great deal of space beside or above the operating table, where other

https://doi.org/10.1017/S0263574714001283 Published online by Cambridge University Press

equipment may be situated. Compared with prismatic joints, rotation joints have good workspace efficiency, defined as the ratio between the workspace and the size of the manipulator. Thus, the 5-DoF SPINEBOT-II (Hanyang University, Korea) has one prismatic joint moving along the edge of the operating table and four rotational joints.[20] However, as previously mentioned, rotational joints in the transverse plane may cause accidental harm to the patient. Furthermore, these robotic systems are designed with 5 DoFs, allowing adjustment of the position and orientation of screw paths during spinal surgery, but with no extra DoF for adjusting the orientation of the tracking marks fixed on the operation tool. Hence, the tracking device, robot, and patient must be placed in precise positions with appropriate posture, otherwise the tracking device sight may be blocked and navigation may fail.

In recent years, three basic control modes have been used in robotic surgery systems: teleoperative, automatic, and cooperative. The teleoperative mode is used in many endoscope-based robotic systems, such as the Da Vinci system.[21,22] The surgeon uses the endoscope to obtain visual information and operate in real-time based on this information. However, most orthopedic surgery robots, including the previously mentioned spinal surgery robots, use computed tomography (CT) or X-ray-image-based navigation to accurately locate the planned position or to move along the planned trajectory. The robots move automatically, guided by navigation information. Robotic surgery systems using the automatic mode include the above-mentioned Spine-Assist (Mazor Robotics, Israel), the URS Evolution 1 (Fraunhofer Institute, Germany), the SPINEBOT-I and SPINEBOT-II (Hanyang University, Korea), the CoRASS (POSTECH, Korea), the Stewart-platform parallel robotic system (HIT, China), and the industrial robot-based systems used by Northwestern University (USA) and the University of Navarra (Spain). Positioning using the image-based automatic mode can be quantitative and more precise compared to manual or teleoperative operation. However, considering the narrow operation area and the complex shape of human vertebrae, the motion of the executive terminal of the robot is not only a point-to-point movement, but also a complete trajectory. Avoiding contact with the patient's body during the robot's movement when using image-based automatic mode still poses a problem.

Robotic surgery systems using the cooperative control mode have been developed to solve this problem. In this mode, cooperative pre-positioning is used before accurate active positioning design. The University of Navarra system uses an admittance control law, which transforms the dragging force into the motion of the the PA-10 robot.[12] In this mode, the surgeon directly drags the end-effector of the robot and the robot moves in the direction of the dragging motion. Therefore, the motion of the robot is controlled by the user in the pre-positioning process, thus avoiding contact with the patient's body. Taylor *et al.* (Watson Research Center, USA) use a similar method of nonlinear mapping from force to speed to improve the control performance of the ROBODOC, a robotics system used in orthopedic surgery.[23] Admittance-based control is the most common method, as most robots only have a position interface. However, problems arise in the vicinity of singularities, where Cartesian position control can typically lead to fast, destabilizing movements.[24] As the DLR-II has torque sensors at the joint level, Albu-Schäffer *et al.* proposed an impedance controller enhanced by local stiffness control for cooperative controlling.[25,26] However, this method conditions the setup of the robot joint. Thus, development of a safer and more efficient cooperative control mode in normal-joint robots is desirable. Furthermore, previous studies have not included a means to comprehensively assess the performance criteria of the cooperative control approaches.

In this paper, we propose a novel RSSS for transpedicular surgery and investigate the kinematics, workspace analysis and optimization, and control strategy of the robotic system in detail. The remainder of the paper is organized as follows. In Section 2, a novel RSSS is proposed and its structure is briefly described. The kinematics, workspace analysis, and optimization of the surgical robot are discussed in Section 3. In Section 4, the control strategy and the comprehensive assessment index for cooperative control are proposed. Experiments are presented in Section 5. Finally, we provide some concluding remarks in Section 6.

2. System Structure of the RSSS

The RSSS contains two main subsystems, the navigation system and the surgical robot. Figure 2 shows the general system structure of the RSSS. The navigation system performs intraoperative tracking

https://doi.org/10.1017/S0263574714001283 Published online by Cambridge University Press

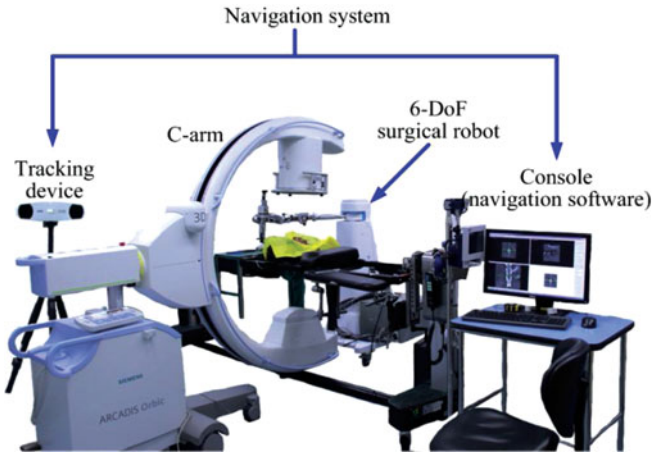

Fig. 2. System structure of the RSSS.

and calculates the movement parameters of the robot. The surgical robot carries out positioning and drilling, assisted by the navigation system.

2.1. Navigation system

The navigation system includes an infrared optical tracking device and navigation software. It fulfills three tasks: tracking the movement of the robot in real-time, providing an interface for surgery planning and sending the planned information to the surgical robot. A C-arm fluoroscopy is used to perform preoperative scanning and obtain medical images of the patient. The scanned images are imported into the navigation software, restructured, and displayed on screen. The surgeons carry out surgical planning via the graphical user interface (GUI) of the navigation software and save the planning information. Intraoperatively, the infrared optical tracker measures position and orientation of the operation device in real-time and sends the information to the navigation software. The movement parameter of the robot is then calculated by the navigation software, using the preoperative planning information and the intraoperative information, and sent to the surgical robot.

2.2. The surgical robot

We propose a novel configuration of a surgical robot (Fig. 3) to satisfy the requirements of spinal surgical operations. The surgical robot is composed of a 6-DoF robotic arm for accurate positioning and an operation tool with one linear DoF for drilling the screw path. A 6-DoF force/torque sensor is mounted on the arm to measure the force and torque acting on the operation tool in real-time. An array of optical marks is fixed on the operation tool to achieve real-time tracking of its position and orientation.

The configuration design of the 6-DoF robotic arm takes into account three significant issues: gravity self-compensation, workspace covering, and tracking occlusion. To implement gravity compensation, the axes of joints 2 and 3 are designed perpendicular to the horizontal plane. These two joints generate the main positioning movement on a sector workspace limited in the horizontal plane. Joint 4 rotates with the axis parallel to the horizontal plane and along the link between joints 4 and 5. The axis of joint 5 is perpendicular to that of joint 4 and parallel to the horizontal plane when joint 4 is in the initial position. The masses of the links between these joints are symmetrically distributed beside the rotational axes. With this configuration, the motion of the robot is restricted in a horizontal work-plane and the effects of gravity on the robotic arm are compensated. With the first prismatic joint, a sector-cylindrical workspace can cover the patient's spine area. An electromagnetic brake is implemented on the first joint to prevent the robotic arm from dropping down in power-off conditions. The direction of the optical marks fixed on the operation tool can be adjusted by the last rotating joint to ensure they face the tracking device, thus avoiding tracking occlusion.

https://doi.org/10.1017/S0263574714001283 Published online by Cambridge University Press

Table I. D–H parameters of the robot.

Links	α_{i-1}	a_{i-1}	θ_i	d_i
1	0	0	0	$d_1(+l_1)$
2	0	l_2	θ_2	0
3	0	l_3	$\theta_3(-\pi/2)$	0
4	$-\pi/2$	0	$\theta_4(-\pi/2)$	l_4
5	$-\pi/2$	0	$\theta_5(-\pi)$	0
6	$-\pi/2$	0	θ_6	l_5

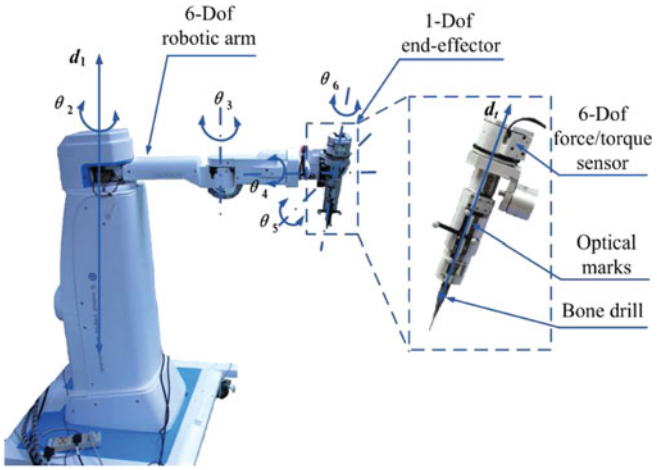

Fig. 3. Structure of the surgical robot.

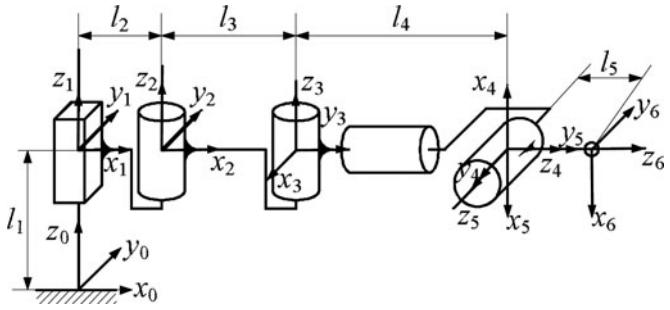

Fig. 4. Coordinates of the robot.

3. Kinematic Analysis

3.1. Forward kinematics

To analyze the kinematics of the surgical robot, the coordinate system of the robotic arm is determined by the D–H method. Figure 4 shows the coordinates of the robot and Table I lists the D–H parameters.

Using these D–H parameters the homogeneous transformation matrix of each joint is formed. The pose matrix of the operation tool can be calculated with the six joint transformation matrices, as shown in Eq. (1).

$$\begin{aligned} \boldsymbol{T}_{\text{kine}} &= {}^{0}\boldsymbol{T}_{6} = {}^{0}\boldsymbol{T}_{1} \cdot {}^{1}\boldsymbol{T}_{2} \cdot {}^{2}\boldsymbol{T}_{3} \cdot {}^{3}\boldsymbol{T}_{4} \cdot {}^{4}\boldsymbol{T}_{5} \cdot {}^{5}\boldsymbol{T}_{6} \\ &= \begin{bmatrix} c_{23}s_5c_6 - s_{23}s_4c_5c_6 - s_{23}c_4s_6 & -c_{23}s_5s_6 + s_{23}s_4c_5s_6 - s_{23}c_4c_6 & s_{23}s_4s_5 + c_{23}c_5 & l_2 + l_3c_2 + l_4c_{23} + l_5(s_{23}s_4s_5 + c_{23}c_5) \\ s_{23}s_5s_6 + c_{23}s_4c_5c_6 + c_{23}c_4s_6 & -s_{23}s_5s_6 - c_{23}s_4c_5s_6 + c_{23}c_4c_6 & s_{23}c_5 - c_{23}s_4s_5 & l_3s_2 + l_4s_{23} + l_5(s_{23}c_5 - c_{23}s_4s_5) \\ s_4s_6 - c_4c_5c_6 & s_4c_6 + c_4c_5s_6 & c_4s_5 & d_1 + l_1 + l_5c_4s_5 \\ 0 & 0 & 0 & 1 \end{bmatrix}. \end{aligned} \tag{1}$$

https://doi.org/10.1017/S0263574714001283 Published online by Cambridge University Press

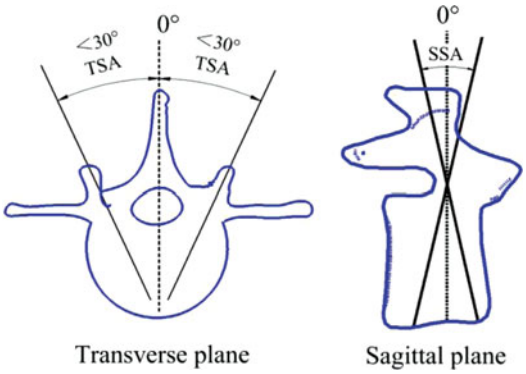

Fig. 5. Requirement analysis of the workspace.

3.2. Inverse kinematics

The process of solving inverse kinematics involves finding the solution to the following equation:

$$\boldsymbol{T}_{\text{kine}} = \boldsymbol{T}_{\text{target}} = \begin{bmatrix} r_{11} & r_{12} & r_{13} & p_x \\ r_{21} & r_{22} & r_{23} & p_y \\ r_{31} & r_{32} & r_{33} & p_z \\ 0 & 0 & 0 & 1 \end{bmatrix}, \tag{2}$$

where T_{target} is the desired target posed matrix of the operation tool. After derivation, the inverse kinematics solutions are obtained by

$$\begin{cases} d_1 = p_z - l_1 - l_5 r_{33} \\ \theta_2 = \text{atan 2}\left(h, \pm\sqrt{(2ml_3)^2 + (2nl_3)^2 - h^2}\right) - \text{atan 2}\left(2ml_3, 2nl_3\right) \\ \theta_3 = \text{atan 2}\left(-n - l_3 s_2, -m - l_3 c_2\right) - \theta_2 \\ \theta_4 = \text{atan 2}\left(s_{23} r_{13} - c_{23} r_{23}, r_{33}\right) \\ \theta_5 = \text{atan 2}\left(\pm\sqrt{1 - (c_{23} r_{13} + s_{23} r_{23})^2}, c_{23} r_{13} + s_{23} r_{23}\right) \\ \theta_6 = \text{atan 2}\left(r_{31} + r_{32}, \pm\sqrt{\alpha^2 + \beta^2 - (r_{31} + r_{32})^2}\right) - \text{atan 2}\left(\beta, \alpha\right) \end{cases}, \tag{3}$$

where $m = l_2 + l_5 r_{13} - p_x$, $n = l_5 r_{23} - p_y$, $\alpha = s_4 + c_4 c_5$, and $\beta = s_4 - c_4 c_5$.

3.3. Workspace analysis

In current navigation-assisted clinical operations, the intraoperative scanning field can cover three contiguous vertebrae. Therefore, the length of the operation area is less than 200 mm and the distance between the two pedicles on each side of a vertebra is less than 130 mm. The expected orientation of the operation tool is shown in Fig. 5. In the transverse plane, the Transverse Screw Angle (TSA) is less than 30°. In the sagittal plane, the sagittal screw angle (SSA) is 0° under normal circumstances.[27] To analyze and describe the workspace, we define the attainable workspace as the space that can be reached by the operation tool. We also define the dexterous workspace as the space that the operation tool can reach with a TSA of –30° and 30°, simultaneously. The maximal available workspace is defined as the maximal rectangle space in the dexterous workspace, and must cover the required operation area in clinical surgery.

From the kinematics and the configuration of the robot, the main factors affecting the attainable, dexterous, and maximal available workspaces are the rotational ranges of joints θ_2, θ_3, θ_4, θ_5 and the lengths of links l_3 and l_4. The relationship and the sensitivity of these factors are analyzed by means of response surface methodology (RSM). The RSM experiments use a Box–Behnken design (BBD), as shown in Table II. The available workspace areas of each group of factors are obtained from 54 experiments. A cubic regression equation is obtained by removing the insignificant terms and is given

https://doi.org/10.1017/S0263574714001283 Published online by Cambridge University Press

Table II. Experimental parameters determined by BBD.

Factors	Low actual	High actual	Low corded	High corded	Mean
θ_2 (°)	70.00	110.00	−1	+1	90.00
θ_3 (°)	90.00	130.00	−1	+1	110.00
θ_4 (°)	60.00	100.00	−1	+1	80.00
θ_5 (°)	20.00	60.00	−1	+1	40.00
l_3 (mm)	350.00	430.00	−1	+1	390.00
l_4 (mm)	360.00	440.00	−1	+1	400.00
Response	Times	Min.	Max.	Mean	S.D.
Ω_i (mm^2)	54	0.00	70400.00	17540.74	21330.07

*$\boldsymbol{\Omega}_i$ is the area of available workspace.

Table III. Optimized factors.

Factors	θ_2	θ_3	θ_4	θ_5	l_3	l_4
Value	100°	130°	63°	60°	350 mm	360 mm
Predicted area			96486.6 mm^2			
Actual area			96,000 mm^2			

by

$$\begin{aligned}\Omega_p = {} & 16455.56 + 27550.00\theta_3 + 7300.00\theta_5 - 4137.50l_4 + 16000.00\theta_3\theta_5 - 2500.00\theta_3\theta_4 \\ & - 4537.50\theta_3\theta_4 - 5162.50\theta_4\theta_5 + 11045.83\theta_3^2 - 8604.17\theta_5^2 - 2900.00\theta_3 l_3 l_4 \\ & - 10725.00\theta_2^2\theta_3 - 4562.50\theta_2^2 l_4 + 9175.00\theta_3^2\theta_5 + 5537.50\theta_3^2 l_4 \,, \end{aligned} \tag{4}$$

where Ω_p is the predicted area of available workspace. Figure 6 shows the response surface of θ_2–θ_5, θ_2–l_3, θ_5–l_3, and θ_5–l_4. The regression equation and the response surfaces indicate that the most sensitive factors affecting the available workspace area are in the rotational range of θ_3 and θ_5. After optimization via the regression equation, the value of each factor is determined (Table III). The area of the predicted available workspace is 96486.6 mm^2, while the actual available workspace is a 640 × 150 mm rectangular box with an area of 96,000 mm^2. Considering the mechanical limitation, the final ranges of these joints and links are determined (Table II). Figure 7 shows the result of the workspace analysis based on the optimized parameters. The red area is the attainable workspace, the middle blue area is the dexterous workspace, and the green inner rectangular box is the available workspace that covers the required operation area. If the movement range of the first prismatic joint is more than 420 mm, the robot's dexterous workspace can cover a 640 × 150 × 420-mm rectangular space, which satisfies the operation space requirement in spinal surgeries.

3.4. Jacobian matrix

The Jacobian matrix of the robot is the basis of cooperative control in both speed and torque modes. The velocity Jacobian matrix maps the velocity from joint space to Cartesian space, while the force Jacobian matrix maps the force/torque acting on the end-effector into the joint space of the robot. Furthermore, the force Jacobian matrix is the transposition of the velocity Jacobian matrix.

The differential-vector method is used to gain the Jacobian matrix of this 6-DoF surgical robot, which is a 6 × 6 matrix:

$$\begin{bmatrix} \boldsymbol{v} \\ \boldsymbol{\omega} \end{bmatrix} = \boldsymbol{J}\dot{\theta} = \begin{bmatrix} \boldsymbol{J}_{L1} & \boldsymbol{J}_{L2} & \boldsymbol{J}_{L3} & \boldsymbol{J}_{L4} & \boldsymbol{J}_{L5} & \boldsymbol{J}_{L6} \\ \boldsymbol{J}_{A1} & \boldsymbol{J}_{A2} & \boldsymbol{J}_{A3} & \boldsymbol{J}_{A4} & \boldsymbol{J}_{A5} & \boldsymbol{J}_{A6} \end{bmatrix} \begin{bmatrix} \dot{d}_1 \\ \dot{\theta}_2 \\ \dot{\theta}_3 \\ \dot{\theta}_4 \\ \dot{\theta}_5 \\ \dot{\theta}_6 \end{bmatrix}. \tag{5}$$

https://doi.org/10.1017/S0263574714001283 Published online by Cambridge University Press

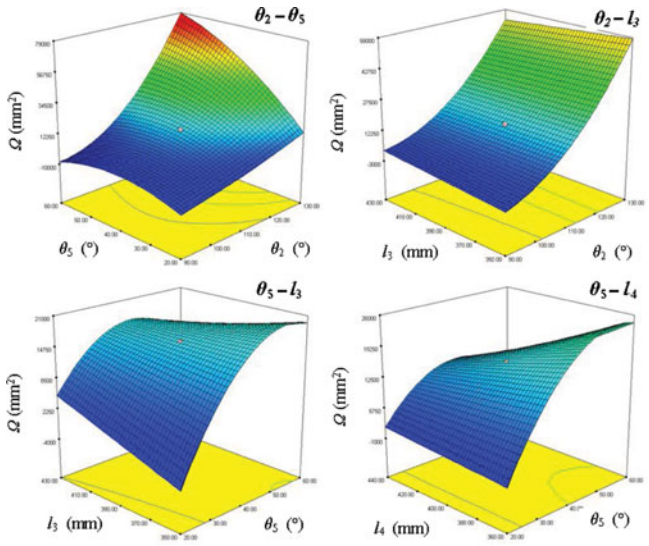

Fig. 6. Response surface of θ_2–θ_5, θ_2–l_3, θ_5–l_3, and θ_5–l_4.

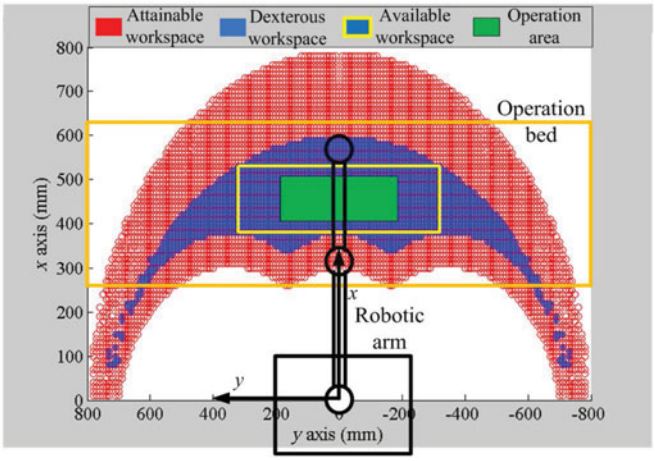

Fig. 7. Workspace analysis.

$[\boldsymbol{J}_{L1}\boldsymbol{J}_{L2}\boldsymbol{J}_{L3}\boldsymbol{J}_{L4}\boldsymbol{J}_{L5}\boldsymbol{J}_{L6}]$ represents the transfer coefficients of linear velocity, which are calculated by the partial-differential of position vector in Cartesian space, as in Eq. (6).

$$\boldsymbol{J}_{Li} = \begin{bmatrix} \dfrac{\partial p_x}{\partial \theta_i} & \dfrac{\partial p_y}{\partial \theta_i} & \dfrac{\partial p_z}{\partial \theta_i} \end{bmatrix}^T. \tag{6}$$

For the transfer coefficients of rotational velocity $[\boldsymbol{J}_{A1}\boldsymbol{J}_{A2}\boldsymbol{J}_{A3}\boldsymbol{J}_{A4}\boldsymbol{J}_{A5}\boldsymbol{J}_{A6}]$, prismatic joints and rotational joints should be considered separately. The movement of the prismatic joint has no effect on the rotation of the end-effector. Therefore, the related element of $\boldsymbol{J}$ is presented as

$$\boldsymbol{J}_{Ai} = [0 \quad 0 \quad 0]^T. \tag{7}$$

The angular velocity of the transfer coefficient for the rotational joints is

$$\boldsymbol{J}_{Ai} = \boldsymbol{Z}_i = {}^0\boldsymbol{R}_i \boldsymbol{Z} = {}^0\boldsymbol{R}_i \begin{bmatrix} 0 \\ 0 \\ 1 \end{bmatrix}, \quad {}^0\boldsymbol{R}_i = \prod_{j=0}^{i-1} {}^j\boldsymbol{R}_{j+1}, \tag{8}$$

https://doi.org/10.1017/S0263574714001283 Published online by Cambridge University Press

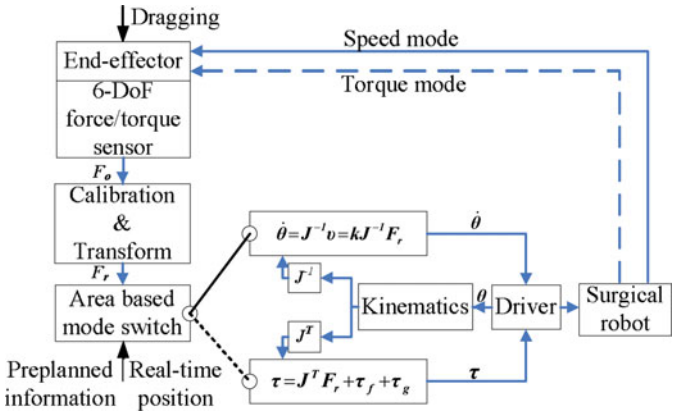

Fig. 8. Cooperative control circle.

where ${}^0\boldsymbol{R}_i$ is the rotational matrix of joint i, and $\boldsymbol{Z}_i$ is the z-axis vector of the rotational matrix. Thus, the velocity Jacobian matrix of the robot is calculated as

$$J=\begin{bmatrix} 0 & -s_2l_3-s_{23}l_4+(-c_5s_{23}+c_{23}s_4s_5)l_5 & -s_{23}l_4+(-c_5s_{23}+c_{23}s_4s_5)l_5 & c_4s_{23}s_5l_5 & (c_5s_{23}s_4-c_{23}s_5)l_5 & 0 \\ 0 & c_2l_3+c_{23}l_4+(c_{23}c_5+s_{23}s_4s_5)l_5 & c_{23}l_4+(c_{23}c_5+s_{23}s_4s_5)l_5 & -c_{23}c_4s_5l_5 & -(c_{23}c_5s_4+s_{23}s_5)l_5 & 0 \\ 1 & 0 & 0 & -s_4s_5l_5 & c_4c_5l_5 & 0 \\ 0 & 0 & 0 & c_{23} & c_4s_{23} & c_{23}c_5+s_{23}s_4s_5 \\ 0 & 0 & 0 & s_{23} & -c_{23}c_4 & c_5s_{23}-c_{23}s_4s_5 \\ 0 & 1 & 1 & 0 & -s_4 & c_4s_5 \end{bmatrix}. \quad (9)$$

4. Control Strategy

For safe and accurate location of the planned position, the robot works in the cooperative control mode for passive positioning and the navigation control mode for active fine adjustment. During the pre-positioning process, the surgeon directly drags the operation tool while in cooperative control mode. The robot's movement follows the surgeon's hand, crosses the narrow incision, avoids collision with the patient's body, and positions the operation tool in the vicinity of the entry point. The robot then switches to the active fine adjustment mode and moves according to information from the navigation system to complete the precise positioning process.

4.1. Hybrid cooperative control

Hybrid cooperative control algorithms, including speed mode and torque mode, are proposed (Fig. 8). The cooperative control circle includes the force/torque sensing, calibration, transformation, and cooperative control algorithms. The process of calibration compensates for the gravity effects of the end-effector. The transformation process transforms the force/torque signals from sensor coordinates to global coordinates. Next, the original control force, $\boldsymbol{F}_o$, of the sensor coordinates is calibrated and transformed into the reference control force, $\boldsymbol{F}_r$, of the global coordinates. The mode switching module is based on the operation areas, which include the speed mode and torque mode areas, generated by the preplanned operation information such as the entry point and the thickness of the patient. The torque mode is used for long displacement and fast movement, while the speed mode is used for precise and low-speed positioning. Consequently, the speed area is set to cover the patient's body and the operation area, while the remainder of the workspace is the torque mode area. The preplanned information and real-time positioning of the robot is provided by the navigation system during the operation.

4.1.1. Cooperative control in speed mode. In the speed mode, the joint motors work in a speed-servo mode. Based on the basic admittance control law $\boldsymbol{v}=\boldsymbol{k}F_r$, where $\boldsymbol{v}$ is the desired Cartesian speed of the robot and $\boldsymbol{k}=\mathrm{diag}(k_1, k_2, k_3, k_4, k_5, k_6)$ is a diagonal matrix to manage the stiffness of motion in

https://doi.org/10.1017/S0263574714001283 Published online by Cambridge University Press

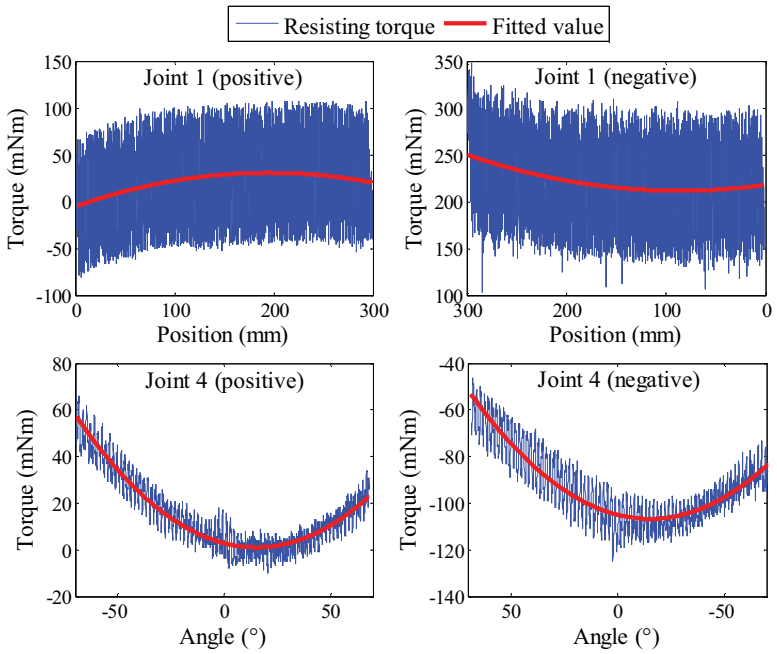

Fig. 9. Effects of friction torque and gravity torque on joints.

each direction, the output joint speed is described as

$$\dot{\theta} = \boldsymbol{J}^{-1}\boldsymbol{v} = \boldsymbol{k}\boldsymbol{J}^{-1}\boldsymbol{F}_{\mathrm{r}}. \tag{10}$$

The robot moves according to this control parameter and performs the cooperative motion by following the motion of the surgeon's hand.

4.1.2. Cooperative control in torque mode. In the torque mode, the joint motors work in a torque-servo mode, and provide proper torque to reduce the effects of friction and gravity. The dragging force directly drives the joints to move, and the control algorithm helps the surgeon to drag the operation tool more easily. The output joint torque is presented as

$$\boldsymbol{\tau} = k_t \boldsymbol{J}^T \boldsymbol{F}_r + \boldsymbol{\tau}_f + \boldsymbol{\tau}_g = k_t \boldsymbol{\tau}_d + \boldsymbol{\tau}_a \tag{11}$$

where $\boldsymbol{\tau}_d$ is the joint driving torque determined by the input dragging force/torque, $\boldsymbol{F}_r$, k_t are scale coefficients, and $\boldsymbol{\tau}_a = \boldsymbol{\tau}_f + \boldsymbol{\tau}_g$ is the assistant joint torque vector combined with the joint friction torque, $\boldsymbol{\tau}_f$, and gravity torque, $\boldsymbol{\tau}_g$. The joint friction and gravity torques are influenced by the direction of rotation and the angle of the joint. Therefore, when the surgeon drags the operation tool, the rotation direction of each joint has to be determined.

We determine the rotation direction of each joint by the dragging force/torque. When the dragging force/torque acts on the operation tool, it generates a driving torque $\boldsymbol{\tau}_d = \boldsymbol{J}^T F_r$ on each joint. $\boldsymbol{J}^T$ is a 6×6 force Jacobian matrix, which is the transposition of the velocity Jacobian matrix. Therefore, the assistant torque of joint i is presented as

$$\tau_{ai} = \begin{cases} \tau_{fi-} + \tau_{gi} \\ \tau_{fi+} + \tau_{gi} \end{cases} = \begin{cases} \tau_{ai-} & \text{for} \quad \tau_{di} < 0 \\ \tau_{ai+} & \text{for} \quad \tau_{di} > 0 \end{cases}, \tag{12}$$

where τ_{di} is the driving torque acting on joint i, and τ_{at+} and τ_{at-} are the assistant torques in the positive and negative rotations of joint i, respectively, which are determined by the Least Square Method based on experimental data. Each joint moves in both the positive and negative directions with a constant velocity. The position and output torque of each joint are shown in Fig. 9.

https://doi.org/10.1017/S0263574714001283 Published online by Cambridge University Press

4.2. Comprehensive assessment index of cooperative control

To evaluate the comprehensive performance of the three methods, speed mode, torque mode, and the hybrid cooperative control mode, a comprehensive assessment index is proposed using the aforementioned four criteria and based on a linear weighting method. It is represented as

$$[y_i]_{3\times1} = [x_{ij}]_{3\times4} \cdot [w_j]_{4\times1}, \tag{13}$$

where y_i is the assessment index of the three contrast groups and x_{ij} are the normalized assessment criteria represented in Eq. (14).

$$[x_{ij}]_{3\times4} = \left[N\left(\frac{1}{\bar{t}_i}\right) N\left(\frac{1}{\bar{e}_i}\right) N\left(\frac{1}{\sigma_i}\right) N\left(\frac{1}{\bar{f}_i}\right) \right]. \tag{14}$$

The average operating time $\bar{t} = [\,\bar{t}_1\ \bar{t}_2\ \bar{t}_3\,]^T$, the average positioning error $\bar{e} = [\,\bar{e}_1\ \bar{e}_2\ \bar{e}_3\,]^T$, the mean-square deviation of error $\sigma = [\,\sigma_1\ \sigma_2\ \sigma_3\,]^T$, and the average operating force $\bar{f} = [\,\bar{f}_1\ \bar{f}_2\ \bar{f}_3\,]^T$ are the criteria measured, where the subscripts 1, 2, and 3 represent the experiments in speed mode, torque mode, and hybrid control, respectively. We use the average operating time $\bar{t}$ and operating force $\bar{f}$ to estimate the difficulty of the cooperative motion, and use the position error $\bar{e}$and its mean-square deviation σ to evaluate the control accuracy.

We use a 4×1 vector $[w_j]_{4\times1}$ to express the weight parameter of $\bar{t}$, $\bar{e}$, σ, and $\bar{f}$, which is written as

$$[w_j]_{4\times1} = k[w_{sj}]_{4\times1} + (1-k)[w_{oj}]_{4\times1}. \tag{15}$$

The weight parameter consists of a subjective part, w_{sj}, and an objective part, w_{oj} $\cdot K \in (0, 1)$ is a coefficient used to manage the ratio of subjective and objective weight. The subjective weight parameter, w_{sj}, was determined after discussion with surgeons. The objective weight parameter, w_{oj}, is calculated by the entropy weight method, as shown in Eq. (16), which obtains a higher weight and thus provides more information.

$$w_{oj} = \frac{(1-s_j)}{\sum_{j=1}^{4}(1-s_j)}, \tag{16}$$

where s_j is the entropy value of the jth criteria and is presented as

$$s_j = -\sum_{i=1}^{3} p_{ij} \ln(p_{ij}), \tag{17}$$

where

$$p_{ij} = {}^{x_{ij}}\Big/\sum_{i}^{3} x_{ij},\ j = 1, 2, 3, 4. \tag{18}$$

4.3. Active fine adjustment mode based on navigation

After coarse positioning in cooperative mode, the RSSS shifts into active fine adjustment mode to achieve fine positioning. Active fine adjustment mode is based on the tracking information and preoperative planning information. The navigation system provides the positions of the pre-planned entry point, ${}^{\mathbf{im}}p_{\mathbf{entry}}$, and target point, ${}^{\mathbf{im}}p_{\mathbf{target}}$, in the image coordinate $\boldsymbol{O}_{\text{Image}}$ and the tracking device tracks the real-time position of the end-effector, ${}^{\text{tr}}\boldsymbol{T}_t$, and the patient, ${}^{\text{tr}}\boldsymbol{T}_p$, in the tracker coordinate $\boldsymbol{O}_{\text{Tracker}}$. This navigation transformation process, shown in Fig. 10, transforms the pre-planned screw path in $\boldsymbol{O}_{\text{Image}}$ into the robot coordinate $\boldsymbol{O}_{\text{Robot}}$. The patient coordinate, $\boldsymbol{O}_{\text{Patient}}$, and $\boldsymbol{O}_{\text{Image}}$ coordinate are matched by the registration process. Therefore, the preoperative planned screw paths in the images are transformed into the operation area on the patient's body. The positions of the entry point, ${}^{\text{rob}}\boldsymbol{p}_{\text{entry}}$,

https://doi.org/10.1017/S0263574714001283 Published online by Cambridge University Press

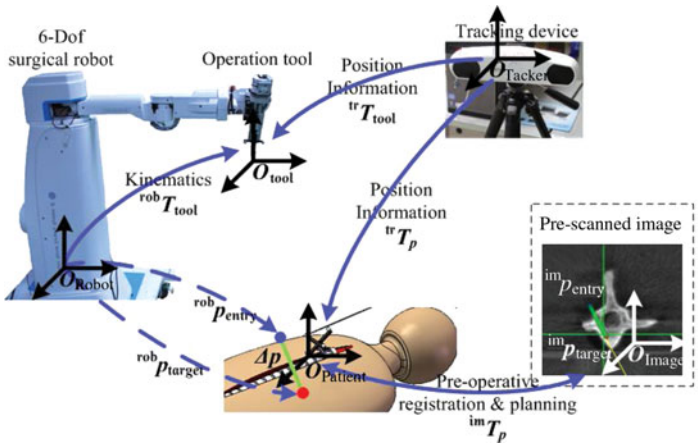

Fig. 10. Process of active fine adjustment.

and target point, ${}^{\text{rob}}\boldsymbol{p}_{\text{target}}$, in the robot coordinate are calculated by

$$\begin{cases} {}^{\mathbf{rob}}\boldsymbol{p}_{\mathbf{entry}} = {}^{\mathbf{rob}}\boldsymbol{T}_{\mathbf{tool}} \cdot {}^{\mathbf{tr}}\boldsymbol{T}_{\mathbf{tool}}^{-1} \cdot {}^{\mathbf{tr}}\boldsymbol{T}_{p} \cdot {}^{\mathbf{im}}\boldsymbol{T}_{p} \cdot {}^{\mathbf{im}}\boldsymbol{p}_{\mathbf{entry}} \\ {}^{\mathbf{rob}}\boldsymbol{p}_{\mathbf{target}} = {}^{\mathbf{rob}}\boldsymbol{T}_{\mathbf{tool}} \cdot {}^{\mathbf{tr}}\boldsymbol{T}_{\mathbf{tool}}^{-1} \cdot {}^{\mathbf{tr}}\boldsymbol{T}_{p} \cdot {}^{\mathbf{im}}\boldsymbol{T}_{p} \cdot {}^{\mathbf{im}}\boldsymbol{p}_{\mathbf{target}} \end{cases}, \tag{19}$$

where ${}^{\mathbf{im}}T_p$ is the registration matrix from $\boldsymbol{O}_{\mathbf{Image}}$ to $\boldsymbol{O}_{\mathbf{Patient}}$, and is gained by means of a point-based registration process, ${}^{\mathbf{tr}}T_p$ is the transformation matrix from $\boldsymbol{O}_{\mathbf{Tracker}}$ to $\boldsymbol{O}_{\mathbf{Patient}}$, ${}^{\mathbf{tr}}\boldsymbol{T}_{\mathbf{tool}}$ is the transformation matrix from $\boldsymbol{O}_{\mathbf{Tracker}}$ to the operation tool coordinate $\boldsymbol{O}_{\mathbf{tool}}$, and ${}^{\mathbf{rob}}{}_{T_{\mathbf{tool}}}$ is the forward kinematics matrix of the robot.

The movement command $\boldsymbol{\Delta p}$ is a position matrix with the position ${}^{\mathbf{rob}}\boldsymbol{p}_{\mathbf{entry}}$ and direction ${}^{\mathbf{rob}}\boldsymbol{p}_{\mathbf{target}}$ as shown in Eq. (20).

$$\begin{gathered} \boldsymbol{\Delta p} = \begin{bmatrix} \mathbf{n} & \mathbf{o} & \mathbf{a} & \mathbf{p} \\ 0 & 0 & 0 & 1 \end{bmatrix}, \\ \boldsymbol{p} = {}^{\mathbf{rob}}\boldsymbol{p}_{\mathbf{entry}} - {}^{\mathbf{rob}}\boldsymbol{p}_{\mathbf{cur}}, a = \frac{{}^{\mathbf{rob}}\boldsymbol{p}_{\mathbf{target}} - {}^{\mathbf{rob}}\boldsymbol{p}_{\mathbf{entry}}}{\left\| {}^{\mathbf{rob}}\boldsymbol{p}_{\mathbf{target}} - {}^{\mathbf{rob}}\boldsymbol{p}_{\mathbf{entry}} \right\|}, \end{gathered} \tag{20}$$

where $\boldsymbol{n}, \boldsymbol{o}, \boldsymbol{a}, \boldsymbol{p}$ represent the 3×1 column vectors of the position matrix and ${}^{\mathbf{rob}}\boldsymbol{p}_{\mathbf{cur}}$ is the current position of the robot. For drilling operations, the orientation is determined by the Euler angles α and β, which can be calculated by $\boldsymbol{a} = [\sin\beta - \sin\alpha\cos\beta\cos\alpha\cos\beta]^{\mathbf{T}}$. The angle γ is set to 0 so that the last joint of the robot can rotate and allow the infrared optical marks to face the tracking device.

5. Experiments and Discussion

Three groups of experiments are performed, including cooperative control experiments, active fine adjustment experiments using a navigation system, and a bone screw insertion experiment.

5.1. Cooperative control experiments

The positioning experiments in the speed mode, torque mode, and hybrid control are performed using the same start and target positions. The measured criteria $\bar{t}$, $\bar{e}$, σ, and $\bar{f}$ are shown in Fig. 11, which indicates that the accuracy and reliability of positioning is better in the speed and hybrid control modes, and that the time cost and dragging force are lower in the torque mode.

Safety is considered the most important factor and is mainly determined by accurate and reliable positioning. A shorter operating time is also desirable. Therefore, the subjective weight parameter, w_{sj}, is determined as [0.2 0.4 0.3 0.1]. The ratio k between the subjective and the objective weight is set as 0.5. Figure 11 shows the comprehensive assessment index of the different control methods. Although the speed mode takes longer and needs a larger dragging force than the torque mode,

https://doi.org/10.1017/S0263574714001283 Published online by Cambridge University Press

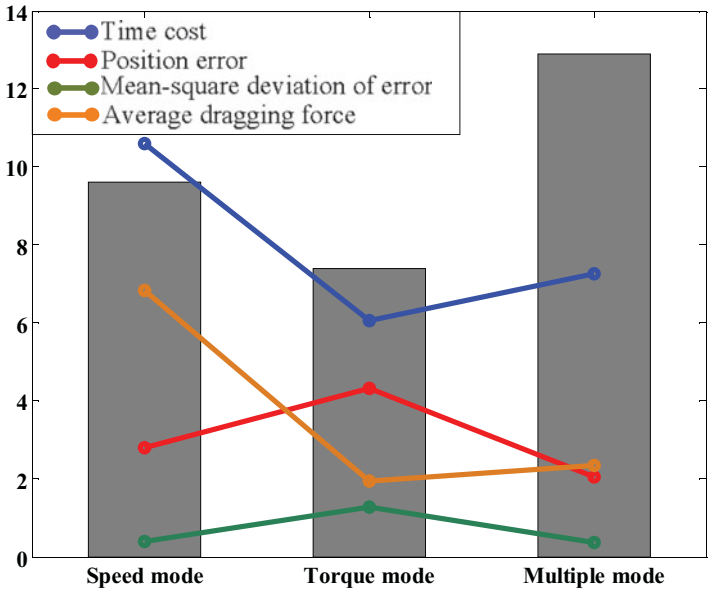

Fig. 11. Comparison analysis of positioning experiments.

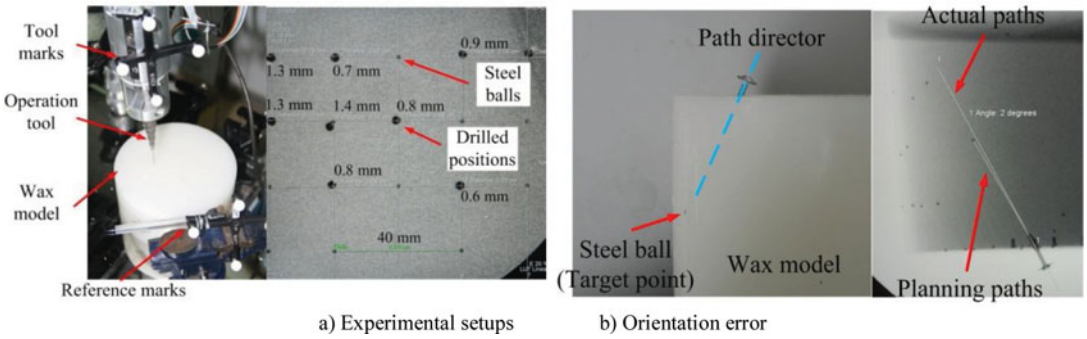

Fig. 12. Results of accuracy experiments.

its positioning error and reliability are superior. The hybrid control mode performs the best, as it combines the advantages of the former two methods in terms of time cost, positioning performance, and operation force.

5.2. Fine adjustment experiments via navigation system

Active fine adjustment experiments are performed using the navigation system. A wax model with an array grid on the surface and side face is used in these experiments. To ensure the cross points of the grid are visible in the C-arm scanned images, steel balls are fixed at these points. In the planning process, the desired entry points of each path are set on the steel balls on the surface of the wax model. The chosen target points are on the side surface of the steel balls, so that the desired paths follow the connection line between the two steel balls. Figure 12(a) shows the planning paths in the navigation system. After planning, the point-based image registration process is carried out, so that the image coordinate matches the coordinate of the wax model. The robot moves to the desired entry point via the desired orientation using the planning paths information. Figure 12(b) shows the results for the C-arm screen after drilling. The positioning accuracy can be evaluated by measuring the length of the line from the planned entry point to the actual entry point on the surface of the wax model. The angle between the desired path and the actual path can be measured from the side view of the wax model. Table IV lists the results of these experiments. The average position error over 20 positionings is about 1.0 mm and the maximal positioning error is 1.3 mm. The average angle error over 10 experiments is 1.1°, and the maximal angle error is 3°.

https://doi.org/10.1017/S0263574714001283 Published online by Cambridge University Press

Table IV. Experimental results.

	Position error (mm)		Angle error (°)
1	1.3	1	1
2	0.7		
3	0.9	2	0
4	1.3		
5	1.2	3	0
6	0.8		
7	0.8	4	2
8	0.9		
9	0.7	5	2
10	0.7		
11	1.2	6	3
12	1.2		
13	1.0	7	1
14	1.2		
15	1.3	8	2
16	0.8		
17	1.2	9	0
18	1.1		
19	1.3	10	0
20	0.8		

Note: Errors are measured by the software of the C-arm. Its measuring accuracy is 0.1 mm for positioning errors and 1° for angle errors.

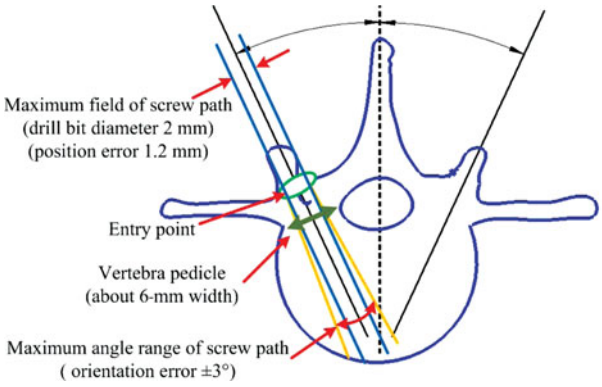

Fig. 13. Accuracy analysis.

The average width of an adult's lumbar vertebra is 7.8–13.4 mm and that of the thoracic vertebra is 6–8.8 mm. The diameter of the drill bit used in these experiments is Φ2 mm. The maximum field of the screw path and the maximum angle of the screw path direction in lumbar surgeries are analyzed in Fig. 13. Assuming the width of the vertebra is 7 mm, from Fig. 13 we can see that a distance of at least 0.8 mm remains from the screw path to the edges of the vertebra pedicle with the maximum position and orientation errors. Therefore, the drilling accuracy satisfies the requirements for all lumbar surgeries and some thoracic vertebrae surgeries.

These position and orientation errors come not only from the robot, but also from the tracking system, calibration process, and registration process. The tracking error, which is approximately 0.4 mm, is determined by the performance of the tracking device. The calibration and registration errors of 0.27 mm and 0.43 mm, respectively, are caused by the operator during the calibration and point-based registration processes. Careful operation during these processes can reduce these errors to a certain extent, but cannot eliminate them completely. In recent clinical operations, automatic

https://doi.org/10.1017/S0263574714001283 Published online by Cambridge University Press

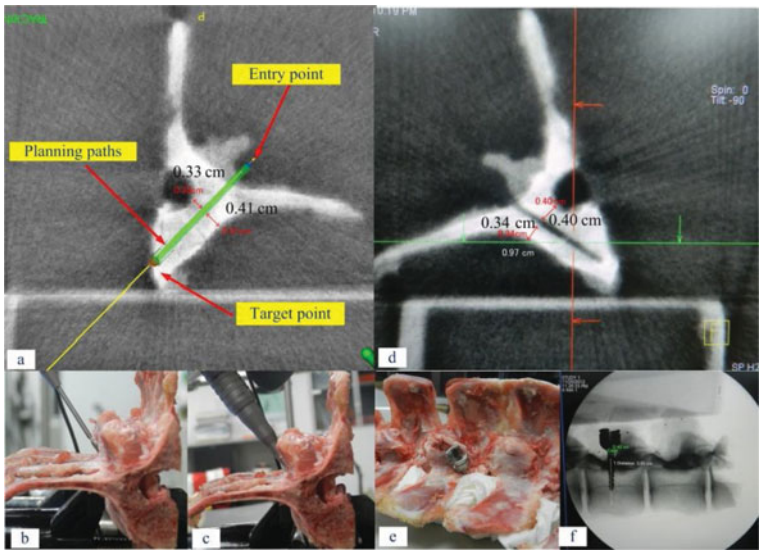

Fig. 14. Bone screw insertion experiment.

registration has been used to remove the effects of human operation. Therefore, future work to improve the accuracy of the RSSS will focus on improving the automatic registration algorithm.

5.3. Bone screw insertion experiment

In this experiment, we use a pig vertebra because of its structural similarity to that of a human. In the planning process, the entry point is selected above the vertebra pedicle, and the target point is in the vertebra body, so that the screw path can cross the center of the pedicle (Fig. 14). After point-based registration the robot is dragged in cooperative control mode and moved to the vicinity of the entry point. The robot is then switched into active fine adjustment mode to perform accurate positioning, guided by the navigation system. From Fig. 14(d) we can see that the screw path is correct in the transverse plane. After inserting a bone screw along the drilled path, Fig. 14(f) shows that the orientation of the path is also correct in the sagittal plane. Therefore, we confirm that the developed RSSS satisfies the objective of the operation sufficiently.

6. Conclusions

We developed an RSSS comprising a 6-DoF surgical robot and an optical navigation system to assist surgeons in carrying out transpedicular surgery. We conducted an intensive investigation of the configuration design and control strategy.

Considering the safety issues involved and the problem of tracking occlusion, we designed a novel 6-DoF surgical robot with one prismatic joint moving along the vertical direction and five rotational joints. Workspace analysis and optimization was based on RSM, to obtain a maximal available workspace that could easily cover the entire operation area with the desired orientation.

In the 6-DoF surgical robotic system, cooperative control for pre-positioning and active control for fine adjustment are used for transpedicular surgery. In the pre-positioning process, the surgeon operates the robot, moving it to the desired position while avoiding contact with the patient's body. Active fine adjustment is applied in our system to guarantee the accuracy via precise navigational information. Combining the speed servo mode and torque servo mode, a hybrid cooperative control method is proposed that achieves both controlled precision and operational dexterity. Furthermore, by means of the measured criteria for average operating time, positioning error, mean-square deviation of error, and average operation force, a comprehensive assessment index based on the entropy weight method is proposed to evaluate the performance of cooperative control algorithms. The experimental results show that the proposed hybrid method performs better in terms of the proposed assessment index. The fine adjustment experiments demonstrate that the positioning accuracy using the navigation

https://doi.org/10.1017/S0263574714001283 Published online by Cambridge University Press

system can meet the requirements of surgeries. A bone screw insertion experiment was performed to test the entire operation process of the RSSS.

Future work will focus on automatic registration to improve the positioning accuracy of our RSSS.

Acknowledgements

This research is supported by the National Natural Science Foundation of China (No. 61175124 and No. 51005227), Key Research Program of the Chinese Academy of Sciences (No. KJZD-EW-TZ-L03), and Guangdong Innovative Research Team Program (No. 201001D0104648280).

References

1. N. Kumar, S. Kukreti, M. Ishaque and R. Mulholland, "Anatomy of deer spine and its comparison to the human spine," *Anatomical Rec.* **260**(2), 189–203 (2000).
2. Q. Li and W. Tian, "Spine Surgery," **In**: *Practice of Orthopaedics* (W. Tian, ed.) (People's Medical Publishing House, Beijing, 2008) pp. 550–560.
3. I. H. Lieberman, D. Togawa, M. M. Kayanja, M. K. Reinhardt, A. Friedlander, N. Knoller and E. C. Benzel, "Bone-mounted miniature robotic guidance for pedicle screw and translaminar facet screw placement: Part I—Technical development and a test case result," *Neurosugery* **59**(3), 641–650 (2006).
4. D. Togawa, M. M. Kayanja, M. K. Reinhardt, M. Shoham, A. Balter, A. Friedlander, N. Knoller, E. C. Benzel and I. H. Lieberman, "Bone-mounted miniature robotic guidance for pedicle screw and translaminar facet screw placement: Part II—Evaluation of system accuracy," *Neurosurgery* **60**(1), 129–139 (2006).
5. S. R. Kantelhardt, R. Martinez, S. Baerwinkel, R. Burger, A. Giese and V. Rohde, "Perioperative course and accuracy of screw positioning in conventional, open robotic-guided and percutaneous robotic-guided, pedicle screw placement," *Eur. Spine J.* **20**(6), 860–868 (2011).
6. C. Stuer, F. Ringel, M. Stoffel, A. Reinke, M. Behr and B. Meyer, "Robotic technology in spine surgery: Current applications and future developments," *Acta Neurochirurgica Suppl.* **109**, 241–245 (2011).
7. H. Tian, D. Wu, Z. Du and L. Sun, "Design and Analysis of a 6-DOF Parallel Robot Used in Artificial Cervical Disc Replacement Surgery," *Proceedings of the 2010 IEEE International Conference on Information and Automation*, Harbin, China (Jun. 20–23, 2010) pp. 30–35.
8. B. Niesing, *Robots for Spine Surgery* (Fraunhofer Magazine, Munich, Germany, 2001) pp. 46–47.
9. S. Kostrzewski, J. M. Duff, C. Baur and M. Olszewski, "Robotic system for cervical spine surgery," *Int. J. Med. Robot. Comput. Assist. Surg.* **8**, 184–190 (2012).
10. J. J. Santos-Munné, M. A. Peshkin, S. Mirkovic, S. D. Stulberg and T. C. Kienzle, "A Stereotactic/Robotic System for Pedicle Screw Placement," *Proceedings of the 3rd Medicine Meets Virtual Reality Conference*, San Diego, USA (1995) pp. 326–333.
11. L. Zagorchev and A. Goshtasby, *Surgical Robot Assistant* (Intelligent System Laboratory, Wright State University, Ohio). Available at: http://www.cs.wright.edu/agoshtas/spine.html.
12. J. Melo, E. Sanchez and I. Diaz, "Adaptive Admittance Control to Generate Real-Time Assistive Fixtures for a COBOT in Transpedicular Fixation Surgery," *Proceedings of the 4th IEEE RAS & EMBS International Conference on Biomedical Robotics and Biomechatronics*, Rome, Italy (Jun. 24–27, 2012) pp. 1170–1175.
13. T. Ortmaier, H. Weiss, S. Dobele and U. Schreiber, "Experiments on robot-assisted navigated drilling and milling of bones for pedicle screw placement international," *J. Med. Robot. Comput. Assist. Surg.* **2**(4), 350–363 (2006).
14. T. Ortmaier, H. Weiss, U. Hagn, M. Grebenstein, M. Nickl, A. Albu-Schaffer, C. Ott, S. Jorg, R. Konietschke, L. Le-Tien and G. Hirzinger, "A Hands-on-Robot for Accurate Placement of Pedicle Screws," *Proceedings of the 2006 IEEE International Conference on Robotics and Automation*, Orlando, USA (May 15–19, 2006), pp. 4179–4186.
15. H. Ju, J. Zhang, G. An, X. Pei and G. Xing, "A Robot-Assisted System for Minimally Invasive Spine Surgery of Percutaneous Vertebroplasty Based on CT Images," *Proceedings of the 2008 IEEE International Conference on Robotics, Automation and Mechatronics*, Pasadena, USA (Sep. 21–24, 2008) pp. 290–295.
16. G. B. Chung, S. Kim, S. G. Lee, B.-J. Yi, W. Kim, S. M. Oh, Y. S. Kim, B. R. So, J. I. Park and S. H. Oh, "An image-guided robotic surgery system for spinal fusion," *Int. J. Control Autom. Syst.* **4**(1), 30–41 (2006).
17. G. B. Chung, S. G. Lee, S. M. Oh, B. J. Yi, W. K. Kim, Y. S. Kim, J. I. Park and S. H. Oh, "Development of SPINEBOT for Spine Surgery," *Proceedings of the 2004 IEEE/RSJ International Conference on Intelligent Robots and Systems*, Sendai, Japan (Sep. 28–Oct. 2, 2004) pp. 3942–3947.
18. J. Lee, I. Hwang, K. Kim, S. Choi, W. K. Chung and Y. S. Kim, "Cooperative robotic assistant with drill-by-wire end-effector for spinal fusion surgery," *Ind. Robot* **36**(1), 60–72 (2009).
19. J. Lee, K. Kim, W. K. Chung, S. Choi and Y. S. Kim, "Human-Guided Surgical Robot System for Spinal Fusion Surgery: CoRASS," *Proceedings of the 2008 IEEE International Conference on Robotics and Automation*, Pasadena, USA (May 19–23, 2008) pp. 3881–3887.

20. S. Kim, J. Chung, B. J. Yi and Y. S. Kim, "An assistive image-guided surgical robot system using O-arm fluoroscopy for pedicle screw insertion: Preliminary and cadaveric study," *Neurosurgery* **67**(6), 1757–1767 (2010).
21. L. W. Sun and C. K. Yeung, "Port Placement and Pose Selection of the da Vinci Surgical System for Collision-Free Intervention Based on Performance Optimization," *Proceedings of the 2007 IEEE/RSJ International Conference on Intelligent Robots and Systems*, San Diego, California (Oct. 29–Nov. 2, 2007) pp. 1951–1956.
22. N. Padoy and G. D. Hager, "Human-Machine Collaborative Surgery Using Learned Models," *Proceedings of the 2011 IEEE International Conference on Robotics and Automation*, Shanghai, China (May 9–13, 2011) pp. 5285–5292.
23. P. Kazanzides, J. Zuhars, B. Mittelstadt and R. H. Taylor, "Force Sensing and Control for a Surgical Robot," *Proceedings of the 1992 IEEE International Conference on Robotics and Automation*, Nice, France (May 12–14, 1992) pp. 612–617.
24. A. Albu-Schaffer and G. Hirzinger, "Cartesian Impedance Control Techniques for Torque Controlled Light-Weight Robots," *Proceedings of the 2002 IEEE International Conference on Robotics and Automation*, Washington, USA (May 11–15, 2002) pp. 657–663.
25. G. Hirzinger, N. Sporer, A. Albu-Schaffer, M. Hahnle, R. Krenn, A. Pascucci and M. Schedl, "DLR's Torque-Controlled Light Weight Robot III – Are We Reaching the Technological Limits Now?," *Proceedings of the 2002 IEEE International Conference on Robotics and Automation*, Washington, USA (May 11–15, 2002) pp. 1710–1716.
26. A. Albu-Schaffer and G. Hirzinger, "A globally stable state feedback controller for flexible joint robots," *Adv. Robot.* **15**(8), 799–814 (2001).
27. T. A. Zdeblick, "Spinal Instrumentation," **In**: *Orthopaedic Knowledge Update: Spine* (S. R. Garfin and A. R. Vaccaro, eds.) (American Academy of Orthopaedic Surgeons, California, 1997) pp. 45–46.

https://doi.org/10.1017/S0263574714001283 Published online by Cambridge University Press